Draft version August 28, 2020
Typeset using LaTeX **twocolumn** style in AASTeX63

Accretion of Gas Giants Constrained by the Tidal Barrier

Ya-Ping Li,[1] Yi-Xian Chen,[2] and Douglas N. C. Lin[3,4]

[1] *Theoretical Division, Los Alamos National Laboratory, Los Alamos, NM 87545, USA*
[2] *Department of Physics, Tsinghua University, Beijing, 100086 China*
[3] *Department of Astronomy & Astrophysics, University of California, Santa Cruz, CA 95064, USA*
[4] *Institute for Advanced Studies, Tsinghua University, Beijing 100086, China*

(Dated: August 28, 2020)

ABSTRACT

After protoplanets have acquired sufficient mass to open partial gaps in their natal protostellar disks, residual gas continues to diffuse onto some horseshoe streamlines under effect of viscous dissipation, and meander in and out of the planets' Hill sphere. Inside the Hill sphere, the horseshoe streamlines intercept gas flow in circumplanetary disks. The host stars' tidal perturbation induce a barrier across the converging streamlines' interface. Viscous transfer of angular momentum across this tidal barrier determines the rate of mass diffusion from the horseshoe streamlines onto the circumplanetary disks, and eventually the accretion rate onto the protoplanets. We carry out a series of numerical simulations to test the influence of this tidal barrier on super-thermal planets. In weakly viscous disks, protoplanets' accretion rate steeply decreases with their masses above the thermal limit. As their growth time scale exceeds the gas depletion time scale, their masses reach asymptotic values comparable to that of Jupiter. In relatively thick and strongly viscous disks, protoplanets' asymptotic masses exceed several times that of Jupiter. Such massive protoplanets strongly excite the eccentricity of nearby horseshoe streamlines, destabilize orderly flow, substantially enhance the diffusion rate across the tidal barrier, and elevate their growth rate until their natal disk is severely depleted. Based on the upper fall-off in the observe mass distribution of known exoplanets, we suggest their natal disks had relatively low viscosity ($\alpha \sim 10^{-3}$), modest thickness ($H/R \sim 0.03 - 0.05$), and limited masses (comparable to that of minimum mass solar nebula model).

Keywords: protoplanetary/protostellar disks, planet-disk interactions, planet accretion

1. INTRODUCTION

A widely adopted theory for planet formation is the core accretion scenario (Bodenheimer & Pollack 1986; Pollack et al. 1996; Ida & Lin 2004). In this theory, giant planets form after the emergence of solid cores through accretion of atmosphere in gas-rich protostellar disks (PSDs). During the quasi-steady accretion phase, the growth of the proto-atmosphere around the cores is driven by slow Kelvin-Helmholtz contraction (Piso & Youdin 2014; Lee et al. 2014; Lee & Chiang 2015; Ormel et al. 2015; Ali-Dib et al. 2020; Chen et al. 2020a). When the atmospheric mass is comparable to the core mass, the atmosphere becomes unstable and the protoplanet transforms into a gas giant through runaway accretion.

In the runaway phase, gas inflow onto the core becomes dynamical. The protoplanet's gravity dominates the flow out to the smaller one of the Bondi radius $R_{\rm B}(= GM_{\rm p}/c_{\rm s}^2$ where $M_{\rm p}$ is the planet's mass and $c_{\rm s}$ is the sound speed in the disk at the planet's semi major axis $a_{\rm p}$) and the Hill radius $R_{\rm H}(\equiv (q/3)^{1/3}a_{\rm p})$ which marks the realm of planet's gravity. For planet-star mass ratio $q(\equiv M_{\rm p}/M_*$ where M_* is the mass of the star) smaller than the thermal limit $q \lesssim q_{\rm th} = 3h_{\rm p}^3$ (where $h_{\rm p} = H/a_{\rm p}$ is the aspect ratio of the disk), we have $R_{\rm B} \lesssim R_{\rm H} \lesssim H$, where $H(= c_{\rm s}/\Omega_{\rm p}$ and $\Omega_{\rm p}$ is the Keplerian angular frequency at $a_{\rm p}$) is the scale height. As more gas is accreted, both the Bondi and the Hill radii increase with q, although the Hill radius grows less steeply. When $q \gtrsim q_{\rm th}$, we have $R_{\rm B} > R_{\rm H} \gtrsim H$.

Corresponding author: Ya-Ping Li, Yi-Xian Chen
leeyp2009@gmail.com, yx-chen17@mails.tsinghua.edu.cn

During their formation, emerging protoplanets tidally interact with their natal disks (Goldreich & Tremaine 1980). Lin & Papaloizou (1986a) shows that tidal perturbation of planets with mass ratio exceeding $q_{\rm th}$ is sufficiently strong to induce the formation of a gap in the disk near the protoplanets' orbits and quench its own growth. If the gas depletion timescale is quite short, the asymptotic mass of gas giants near the ice line in PSDs similar to the Minimum Mass Solar Nebula (MMSN) are comparable to that of Jupiter (Lin & Papaloizou 1993; Bryden et al. 1999).

On the other hand, many hydrodynamical simulations show that gas continues to flow across the planet's orbit even after the planet reaches the gap-opening mass (Lubow et al. 1999; Kley et al. 2001; Duffell & MacFadyen 2013; Fung et al. 2014; Dürmann & Kley 2015). The diffusion of incoming materials across the gap maintains a steady gas profile with a certain minimum density. Attempts have been made to analytically and empirically model such steady gap profiles (Kanagawa et al. 2015; Duffell 2015; Ginzburg & Sari 2018; Duffell 2020), and these gap prescriptions have been applied to infer gas giant planets' growth limit in the modified gap-opening paradigm (Tanigawa & Ikoma 2007; Tanigawa & Tanaka 2016; Ginzburg & Chiang 2019; Rosenthal et al. 2020). The asymptotic mass (if in disks with moderate viscosity) obtained in these studies is typically an order of magnitude higher than previously estimated, and they predict an excess of 10 $M_{\rm J}$ planets around solar-type star systems. The prolific production of such high-mass planets is incompatible with the observed ceiling in the mass distribution obtained from radial velocity surveys of long-period planets (Marcy et al. 2005; Cumming et al. 2008; Mayor et al. 2011; Petigura et al. 2018).

In contrast, Dobbs-Dixon et al. (2007) has shown that despite the residual flow through the gap, the gas may not be so efficiently accreted onto the protoplanets. In general, the protoplanet's physical radius is much smaller than either $R_{\rm B}$ or $R_{\rm H}$. It is surrounded by a circumplanetary disk (CPD) supplied by gas from the PSD via horseshoe streamlines. In an inviscid or weakly viscous disk, the vortensity and Bernoulli energy are fully or mostly conserved along streamlines (Korycansky & Papaloizou 1996; Balmforth & Korycansky 2001). In addition, there is a vortensity mismatch between the horseshoe streamlines and the outer region of CPD. Under the influence of the host stars' tidal perturbation and the Coriolis force in the frame corotating with the planet, a tidal barrier is established across the interface where flows converge. Although turbulence or weak shocks lead to angular momentum transfer and energy dissipation along the interface where they converge, the mass transfer rate from the horseshoe streamlines to the CPDs is restrained in the low-viscosity limit. This inflow is the source of gas supply to the accreting protoplanets.

This tidal barrier effect has been analyzed by Dobbs-Dixon et al. (2007). In both of their simulated models, there is no explicitly specified viscosity other than the inherent numerical viscosity in their computational scheme. In this paper, we carry out an extensive series of numerical simulations to verify the validity of their tidal barrier conjecture in the low-viscosity limit and and show that it is marginalized in the high-viscosity limit. We evaluate the gas giants' accretion rates for some ranges of relevant model parameters. In §2, we briefly recapitulate the results from previous investigators. In §3 we introduce the numerical setup of our simulations, and in §4 we discuss our numerical results. We explore different parameter spaces of α and $h_{\rm p}$ to compare our own numerical results on accretion rates with the predictions extrapolated from various prescriptions. We use tracers velocity field lines and vortensity contours to show the effectiveness of the tidal barrier. In §5 we give a summary of our findings and discuss their implications.

2. PREVIOUS SEMI-ANALYTIC ESTIMATES AND NUMERICAL RESULTS

In the classical scenario, tidal interaction between a gap-opening planet and the surrounding disk induces an exponentially deep gap, enough to disconnect the inner disk and outer disk (Lin & Papaloizou 1986a), and quench gas flow across the gap as well as the accretion onto the planet (Bryden et al. 1999; Crida et al. 2006). However, e.g.Lubow et al. (1999) showed that there is residual gas in the gap even for planets with $q \geq q_{\rm th}$. In general, the azimuthally averaged surface density attains a minimum value $\Sigma_{\rm min}$ at the planet's orbital semi major axis $a_{\rm p}$. In the two dimensional limit, a finite residual $\Sigma_{\rm min}$ can supply an embedded planet an accretion rate of

$$\dot{m}_{\rm p} = A\Sigma_{\rm min}. \tag{1}$$

Based on their numerical simulations, Tanigawa & Watanabe (2002) fitted an empirical formula for the accretion coefficient A

$$A = 0.29{h_{\rm p}}^{-2} q^{4/3} a_{\rm p}^2 \Omega_{\rm p}. \tag{2}$$

Apart from A, we still need an estimate for the gas surface density inside the gap region to calculate $\dot{m}_{\rm p}$. With a global numerical scheme, Duffell & MacFadyen (2013) simulated tidal interaction between planets and their natal disks for several $M_{\rm p}$, α, and $h_{\rm p}$. They empirically obtained a formula for the characteristic gas

surface density in the gap region:

$$\frac{\Sigma_{\rm min}}{\Sigma_{\rm p}} = \frac{1}{1+0.034K}, \quad \text{where} \quad K = q^2 h_{\rm p}^{-5} \alpha^{-1}. \quad (3)$$

Partial disk clearing is also confirmed by Fung et al. (2014) and Dürmann & Kley (2015).

This reduction factor in the magnitude of Σ has also been consistently approximated using semi-analytical approaches by Fung et al. (2014); Kanagawa et al. (2015). With this estimate of $\Sigma_{\rm min}$ as well as the estimate of A from Tanigawa & Watanabe (2002), Tanigawa & Tanaka (2016) obtains a full prescription for the planetary accretion rate (hereafter, it is referred to as the TT formula). Their predicted mass accretion rate for $\alpha = 0.004$ and $h_{\rm p} = 0.05$ at $a_{\rm p} = 5.2$ au is plotted in Figure 1.

For comparison, we have also shown (in Figure 1) the normalized planetary accretion rates from three independent 3D simulations carried out by D'Angelo et al. (2003) (blue, different symbols represent different smoothing potentials) and Bodenheimer et al. (2013) (red), analogous to Figure 1 of Tanigawa & Tanaka (2016). There are apparently some deviations in the accretion rates obtained from D'Angelo et al. (2003); Bodenheimer et al. (2013) (with exactly the parameters $\alpha = 0.004$ and $h_{\rm p} = 0.05$) compared to the TT formula. In particular, when the planet is above the thermal mass, the numerical steady accretion rate follows a steeper decline - this discrepancy is much more evident in comparison with Bodenheimer et al. (2013)'s results.

Tanigawa & Tanaka (2016) suggested the simulated results of Machida et al. (2010) might support their prediction that the accretion rate does not fall off steeply above $q_{\rm th}$, but their set of simulations used an inviscid disk (with $h_{\rm p} = 0.05$ but physical viscosity $\alpha \approx 0$), in which $\Sigma_{\rm min}$ should not be approximated by Equation 3. Rather, it might fit into the "inviscid and sub-thermal" regime discussed by Ginzburg & Sari (2018) and is expected to give smaller bottom density and smaller accretion rate. Ginzburg & Chiang (2019) applied this inviscid scalings to obtain the final masses of gas giants and found they are generally low ($\lesssim M_{\rm J}$), but they also clarified that this scaling suffers from inaccuracies for super-thermal planets with small $h_{\rm p}$ (see their §3.2.4). We do not attempt to apply this scaling to account for Machida et al. (2010)'s results, since we will be focusing on the moderate-viscosity, super-thermal regime where the Duffell & MacFadyen (2013); Kanagawa et al. (2015) formula is usually practically applied [1].

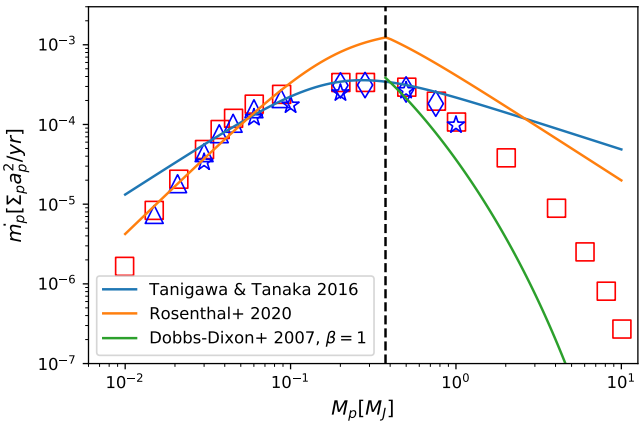

Figure 1. Planetary accretion rates as a function of planet mass. Different color curves indication predictions of planet accretion rate, in units of disk mass per year, as functions of planet mass $M_{\rm p}$ for a specific $h_{\rm p} = 0.05$ and $\alpha = 0.004$. Different blue triangles and stars represent D'Angelo et al. (2003)'s data points with different smoothing potential models. The red squares are the results from Bodenheimer et al. (2013)

In another semi-analytic approach, Rosenthal et al. (2020) used simple Bondi and Hill radii to approximate the accretion radius of planets with sub-thermal and super-thermal masses respectively. We refer this prescription as the RCGM formula. Since for Bondi accretion $\dot{m}_{\rm p} \sim \Sigma_{\rm min} c_{\rm s} R_{\rm B}^2 / H$ (Frank et al. 1992) and for Hill sphere accretion $\dot{m}_{\rm p} \sim \Sigma_{\rm min} R_{\rm H}^2 \Omega_{\rm p}$, they obtain

$$A = \begin{cases} A_{\rm Bondi} = c_1 \dfrac{q^2}{h_{\rm p}^4} \Omega_{\rm p} a_{\rm p}^2 & q < q_{\rm th} \\ A_{\rm Hill} = c_2 q^{2/3} \Omega_{\rm p} a_{\rm p}^2 & q > q_{\rm th} \end{cases} \quad (4)$$

and fit the order-unity coefficients c_1 and c_2 with numerical results. They assume that Hill accretion and Bondi accretion continuously connect at around the thermal mass $q_{\rm th}$. Rosenthal et al. (2020) obtains a result of $c_1 = 0.5$ and $c_2 = 2.2$ by calibrating the factors according to D'Angelo et al. (2003)'s 3D results. Practically, they adopted a formula similar to Equation 3 as an estimate of $\Sigma_{\rm min}$ for gap-opening planets (see their

[1] We note that the original data from Figure 5 of Machida et al. (2010) is rescaled by a factor of 2 when plotted in Figure 1 of Tanigawa & Tanaka (2016), although their vertical axis is both $M_{\rm J}$/yr in a standard MMSN disk ($\Sigma = \sqrt{2}\rho H \approx 140 {\rm g \cdot cm^{-2}}$ at 5 au, ρ, Σ is the gas 3D & 2D density). The reason for this discrepancy is unclear.

Equations 24-27). Their scaling of $\dot{m}_{\rm p}$ is also shown in Figure 1 for disk viscosity $\alpha = 0.004$ and aspect ratio at the planet $h_{\rm p} = 0.05$.

In comparison with the TT prescription, RCGM prescription follows a steeper decline with q. Nevertheless, it over-predicts the accretion rate for gap-opening planets compared to numerical results of D'Angelo et al. (2003); Bodenheimer et al. (2013). In fact, if gap-opening planets accrete at the rates predicted by either prescriptions, the mass doubling timescale would be $\tau_{\rm p} = M_{\rm p}/\dot{m}_{\rm p} \sim 10^4 - 10^5$ years for a Jupiter-mass planets at $r_{\rm p} = 5$ au in a MMSN. If their natal disks deplete over a characteristic timescale of $\tau_{\rm dep} \sim 1-3$ Myrs, the asymptotic mass of proto gas giant planets would typically be $\gtrsim 10\ M_{\rm J}$. Such an extrapolation would be difficult to reconcile with the apparent ceiling (a sharp decline in numbers for planet mass larger than a few $M_{\rm J}$) of the planetary mass distribution (Cumming et al. 2008; Marcy et al. 2005; Mayor et al. 2011; Petigura et al. 2018).

In order to get around this excess mass issue, Tanaka et al. (2020) suggested that runaway gas accretion occur in advanced stages of protostellar evolution, just prior to the rapid depletion of disk gas. Although transitional photoevaporation of the disk (Owen et al. 2011) may be a possible culprit. Fine tuning in the timing and duration of disk depletion episodes is needed to account for the commonly found Jupiter-mass long-period planets. Such requirements may not be compatible with the ubiquitous gap structures in PSDs (Andrews et al. 2018; Long et al. 2018). Small $\tau_{\rm p}(< 1$ Myr) also poses challenges to the formation of multiple Jupiter-mass planets around the same host stars, unless they are coeval within some brief time intervals ($< \tau_{\rm p}$).

One way to quench accretion rate is to have more severe gas depletion in the gap. But as long as there is sufficient gas flow across the gap, a finite residual surface density is still maintained such that the scaling in Equation (3) (Duffell & MacFadyen 2013; Kanagawa et al. 2015) would be order-unity accurate. Severe depletion of the gap can only occur in the limit of $q \gg q_{\rm th}$. A complete cutoff in the gas flow across the planets' orbit also leads to the classical type II migration (Lin & Papaloizou 1986b; Lin et al. 1996). Omnipresence of extensive migration (coupled with the viscous evolution of the disk) would lead to an overpopulation of hot Jupiters which is not consistent with the observed period distribution(Ida et al. 2013). The preservation of some residual gas flow across the gap may reduce the rate of type II migration and help the retention of cold Jupiters (Chen et al. 2020b).

The above analytical or empirical formulae neglect the tidal effects due to the non-axisymmetric potential in the proximity of the planets' Hills radius. In the frame corotating with the planet's orbit, the equipotential surfaces are characterized by the L_1 saddle point which demarcates the Hills radius as well as the L_4 and L_5 Trojan (local maxima) points around which horseshoe streamlines circumvolve. In addition to the host stars' tidal perturbation, gas flow is also subjected to the Coriolis effects. In the proximity of the planet, gas cross the gap in horseshoe streamlines. Although its angular momentum varies, vortensity and Bernoulli energy of the gas are conserved along streamlines in the inviscid limit (Korycansky & Papaloizou 1996; The Bernoulli energy is equivalent to Jacobi energy in the restricted 3-body problem Murray & Dermott (1999))

The tidal perturbation of planets with $q \ll q_{\rm th}$ on the gas flow is generally weak near their Hills radius. Its gravity is only important inside the Bondi radius. After planets have acquired a thermal mass (with $q \gtrsim q_{\rm th}$), the tidal and Coriolis forces deflect the horseshoe streamlines which enter into the planets' Hill sphere and prevent them from directly striking the planets' physical radius. In fact, the vortensity of the horseshoe streamlines does not match those on the outer region of the CPD (Korycansky & Papaloizou 1996). Viscous transport of angular momentum and energy dissipations are needed to cross the interface which separate these regions (Balmforth & Korycansky 2001). The protracted presence of residual gas along the streamlines in the gap region does not necessarily imply that it would be efficiently accreted onto the protoplanet.

This subtle effect is neglected in the TT and RCGM prescriptions. Their assumption that $\Sigma_{\rm min}$ azimuthal distribution is uniform implicitly assumes that the viscous transport and dissipation has smeared out the horseshoe streamlines. Dobbs-Dixon et al. (2007) emphasize the importance of this effect in the inviscid limit. They showed that, for Hill accretion conserving the Bernoulli energy and vortensity (see their Eqn 28):

$$A_{\rm Hill} \approx 2\pi R_{\rm H} H \Omega_{\rm p} \exp\left[-\beta\left(\frac{R_{\rm H}}{H}\right)^2 - \frac{1}{2}\right] \qquad (5)$$

where β is an order-unity empirical factor. We refer this approach as the DLL prescription. This modification from the expression of $A_{\rm Hill}$ in Equation (4) becomes large in the limit $R_{\rm H} > H$ i.e. when the protoplanets' mass is above the thermal limit. The important implication of this expression is that the protoplanets' accretion rate decays exponentially with some power of q.

The main physical reasons for this transition to inefficient planetary accretion are: 1) the fraction of gas

on the horseshoe streamlines which can reach, in azimuth, the planet's Hills sphere before making a U-turn decreases with the planet's q. 2) The differences in the magnitude of both vortensity (Papaloizou & Lin 1989) and Bernoulli energy between the horseshoe and CPD flows increase with the planet's q. 3) While both vortensity and Bernoulli energy are conserved along the streamlines in the inviscid limit (Korycansky & Papaloizou 1996; Balmforth & Korycansky 2001), flow from the horseshoe streamlines into the protoplanet's Hill's sphere and gas accretion onto the CPD requires shock dissipation. Consequently, only a fraction of the gas passing through this region is retained. The inviscid numerical simulations (Dobbs-Dixon et al. 2007) confirmed this barrier. But the effect of additional diffusing enabled by intrinsic turbulent viscosity (other than implicit numerical viscosity) has yet to be investigated.

In order to contrast the difference between the three prescriptions, we have also plotted this prediction (Eqn 5) in Figure 1 (green), for the empirical value of $\beta \sim 1$. The predictions of three accretion rate estimates diverge at the high values of q, albeit their differences are small for Jupiter-mass planets. For $M_{\rm p} > M_{\rm J}$, we only have results from Bodenheimer et al. (2013) for comparison for disk parameters $h_{\rm p} = 0.05$, $\alpha = 0.004$, whose fall-off slope conforms more with DLL than TT and RCGM prescriptions. The excess accretion rate observed in simulations can be naturally accounted for by non-negligible viscous dissipation.

However, the numerical simulations shown in Figure 1 are performed with viscosity. As we will show below that viscous stress can lead to angular momentum transfer between different streamlines and cause deviations from DLL scaling. In addition to intrinsic viscosity, artificial angular momentum transfer may also be introduced by the boundary condition and spacial resolution in different numerical algorithms. Dobbs-Dixon et al. (2007) have pointed out that the 2D local-coordinate (with repeated boundary condition across an azimuthal patch centered on the planet) simulations of Tanigawa & Watanabe (2002) might not be adequate to capture a gap-opening planet's secular perturbation on the global gas flow patterns. For the nested-grid coordinates in the 3D simulations of D'Angelo et al. (2005); Machida et al. (2010); Bodenheimer et al. (2013), the resolution for gas flows at azimuth locations far from the planet is also coarse. It is possible that certain global effects might have been overlooked. In high resolution 2D simulations (with uniform grids), a very important finding is that when a planet's q reaches $\gtrsim 0.003-0.005$, the eccentricity of disk gas streamlines is excited to $\gtrsim 2H/a_{\rm p}$. The radial excursion of streamlines bring external gas well into the gap. Streamline crossing inside the planet's Hill radius also leads to shocks, enhancing vortensity diffusion and energy dissipation. Consequently, the accretion rate of these relatively massive planet is elevated (Kley & Dirksen 2006; Regály et al. 2010; Duffell & Chiang 2015; Teyssandier & Ogilvie 2016, 2017). In this case, the scalings for stable accretion on circular orbits is no longer appropriate.

Nevertheless, protoplanets can self-consistently acquire an asymptotic mass $M_{\rm p} \lesssim 3-5\ M_{\rm J}$ without significantly exciting the eccentricity of the streamlines near their orbits, provided that they form in regions of their natal disk with relatively small thickness (and therefore a modest thermal mass limit). In relatively thick regions of the disk where their thermal mass exceeds the threshold mass for the excitation of significant streamline eccentricity, their asymptotic mass is reached when the nearby regions of the disk is severely depleted. This outcome can lead to even higher terminal masses than those estimated by Tanigawa & Tanaka (2016); Rosenthal et al. (2020). This extrapolation directly contradicts Bodenheimer et al. (2013)'s results, which do no show a rise in accretion rate even for 10 $M_{\rm J}$ planets. In our global high resolution runs (see discussion in §4.2), we have also identified eccentricity growth in the disk that induces high accretion rate for large mass planets. In this regime, the flow structure around the planet becomes more complicated, and theories of stable accretion would no longer be applicable. Although the results of D'Angelo et al. (2003); Bodenheimer et al. (2013) seems to support exponential decay of accretion rates for Jupiter-mass protoplanets, the causes (physical or computational) for dichotomy between the 2D and 3D simulations for high-mass planets need to be cautiously revisited.

3. NUMERICAL METHOD

3.1. *Hydrodymamical Model*

In our simulations with `LA-COMPASS` (Li et al. 2005, 2009), we use a thin and non-self-gravitating PSD. We choose a 2D cylindrical coordinate system (r, φ), and the origin locates at the position of the central star with mass M_*. We adopt a simple model in which the PSD's temperature is independent of the distance above the midplane $T_{\rm disk} \propto r^{-\zeta}$ with aspect ratio

$$h = \frac{c_{\rm s}}{v_{\rm K}} = \frac{H}{r} = h_{\rm p} \left(\frac{r}{a_{\rm p}} \right)^{(1-\zeta)/2} \tag{6}$$

where $v_{\rm K}$ is the Keplerian velocity, $c_{\rm s}$ is the sound speed, and $a_{\rm p}$ is semi major axis of the planet's circular orbit. We take the natural units of $G = M_* = a_{\rm p} = 1$. The

Table 1. Model parameters and planetary accretion rates

model	$q/10^{-3}$	$\Sigma_{\rm p}$ $(M_*/a_{\rm p}^2)$	α	$h_{\rm p}$	Δ $(R_{\rm H})$	f/τ $(\Omega_{\rm p})$	$\dot{m}_{\rm p}$ $(\Sigma_{\rm p}a_{\rm p}^2\Omega_{\rm p})$	Comments
a03h03m025	0.25	10^{-3}	1.11×10^{-3}	0.03	0.1	5.0	7.0×10^{-6}	
a02h03m1	1.0	–	1.11×10^{-2}	0.03	–	–	5.0×10^{-5}	
a03h03m1	1.0	–	1.11×10^{-3}	0.03	–	–	6.5×10^{-7}	
a02h05m1	1.0	–	1.11×10^{-2}	0.05	–	–	2.5×10^{-4}	
a03h05m1	1.0	–	1.11×10^{-3}	0.05	–	–	1.0×10^{-5}	
a02h03m1rs	1.0	–	1.11×10^{-2}	0.03	0.05	5.0	4.5×10^{-5}	convergence
a02h03m1ta	1.0	–	1.11×10^{-2}	0.03	0.1	2.0	4.5×10^{-5}	tests
a02h03m1d	1.0	10^{-4}	1.11×10^{-2}	0.03	–	–	5.0×10^{-5}	
a02h03m2	2.0	–	1.11×10^{-2}	0.03	–	–	3.0×10^{-5}	
a03h03m2	2.0	–	1.11×10^{-3}	0.03	–	–	$(0.5-10)\times10^{-7}$	unstable eccentricity
a02h05m2	2.0	–	1.11×10^{-2}	0.05	–	–	1.5×10^{-4}	
a03h05m2	2.0	–	1.11×10^{-3}	0.05	–	–	2.0×10^{-6}	
a02h03m4	4.0	–	1.11×10^{-2}	0.03	–	–	1.0×10^{-5}	
a03h03m4	4.0	–	1.11×10^{-3}	0.03	–	–	$(1.0-5.0)\times10^{-5}$	unstable eccentricity
a02h05m4	4.0	–	1.11×10^{-2}	0.05	–	–	8.0×10^{-5}	
a03h05m4	4.0	–	1.11×10^{-3}	0.05	–	–	$(1.0-3.0)\times10^{-5}$	unstable eccentricity
a02h03m6	6.0	–	1.11×10^{-2}	0.03	–	–	$(2.0-20.0)\times10^{-5}$	unstable eccentricity
a02h05m6	6.0	–	1.11×10^{-2}	0.05	–	–	6.0×10^{-5}	
a02h05m8	8.0	–	1.11×10^{-2}	0.05	–	–	$(1.0-2.0)\times10^{-4}$	unstable eccentricity

disk has an initial profile of

$$\Sigma(r) = \Sigma_{\rm p}\left(\frac{r}{a_{\rm p}}\right)^{-s}, \tag{7}$$

where $\Sigma_{\rm p}$ is the surface density at the orbital radius of the planet, with a natural unit of $M_*/a_{\rm p}^2$. The 2D velocity vector of the gas is $\vec{v} = (v_r, v_\varphi)$, and angular velocity is $\Omega = v_\varphi/r$.

We numerically solve the vertically integrated continuity equation and the equation of motion in a non-rotating frame centered on the host star. In calculating the gravitational potential of the planet at $\vec{r}$, we use a smoothed potential of the form (e.g. Goldreich & Tremaine 1980)

$$\phi_{\rm p} = -\frac{GM_{\rm p}}{(|\vec{r}_{\rm p}-\vec{r}|^2+\epsilon^2)^{1/2}} + q\Omega_{\rm p}^2\vec{r}_{\rm p}\cdot\vec{r} \tag{8}$$

where $\vec{r}_{\rm p}$ indicates the location of the planet, $\epsilon = 0.4\ R_{\rm H}$ is the softening length. The second term on the right hand side of the above equation corresponds to the indirect term associated with the host star's motion relative to the center of mass. Without the loss of generality, we can consider a solar-type host star with $M_* = M_\odot$ and therefore $q = 0.001$ corresponds to a planet mass of $M_{\rm p} = M_{\rm J}$.

We use the damping boundary condition (de Val-Borro et al. 2006) to provide wave killing zones at each radial edge of the disk to prevent wave reflections. We adopt the conventional α prescription for the kinematic viscosity $\nu = \alpha c_{\rm s} H$ (Shakura & Sunyaev 1973). In disk regions where distance to the star r is much smaller than the characteristic disk size, the radial velocity and disk accretion rate due to viscous diffusion are given as (see Frank et al. 1992, for a review):

$$v_r \sim \frac{3\nu}{2r} \tag{9}$$

$$\dot{M}_* \sim 3\pi\nu\Sigma = 3\pi\alpha h_{\rm p}^2 a_{\rm p}^2\Sigma_{\rm p}\Omega_{\rm p}\cdot\left(\frac{r}{a_{\rm p}}\right)^{1.5-s-\zeta} \tag{10}$$

In a steady state disk without a planet, $\dot{M}_*$ is independent of r. This state is established with $s+\zeta = 1.5$. In this study, we fix $s = 1.0$ and $\zeta = 0.5$ for the unperturbed disk (i.e. the initial distribution without the protoplanet's tidal perturbation). We set the outer boundary of the computational domain to be much larger than $a_{\rm p}$ and impose a steady mass influx with appropriately extrapolated values of $\Sigma(r)$ and $h(r)$.

In our main runs, we set the fiducial gas surface density $\Sigma_{\rm p} = 10^{-3}$. This corresponds to $\Sigma_{\rm p} = 356\ {\rm g\cdot cm^{-2}}$, which is 2-3 times larger than the MMSN value (Hayashi 1981), for $M_* = M_\odot$ and $a_{\rm p} \sim 5$ au. In natural units, the accretion rate is $8.5\times10^{-9}(h_{\rm p}/0.03)^2(\alpha/0.001)M_*\Omega_{\rm p}$ and corresponds to $4.8\times$

$10^{-9}(h_{\rm p}/0.03)^2(\alpha/0.001)M_\odot$ yr^{-1} for the Jupiter case of $M_* = M_\odot$ and $a_{\rm p} \sim 5$ au. Nevertheless, we note that when the accretion rate is measured in scale-free units $\Sigma_{\rm p}a_{\rm p}^2\Omega_{\rm p}$ or $\Sigma_{\rm p}a_{\rm p}^2$/yr, any initial $\Sigma_{\rm p}$ will yield similar results as long as the disk has negligible self-gravity, in our case for $h_{\rm p} > 0.03$.

3.2. *Planetary Accretion*

In order to simulate planetary accretion, we follow Tanigawa & Watanabe (2002); D'Angelo et al. (2003); Dobbs-Dixon et al. (2007) and introduce a small sink-hole (with a radius Δ) centered around the planet. We reduce the central surface density $\Sigma_{\rm c}$ of the gas by a factor of f over some time interval τ. The magnitude of $\Sigma_{\rm c}$ is determined by gas flow patterns at the planetary proximity and it might be quite different from the average surface-density minimum ($\Sigma_{\rm min}$) in the gap. The planet accretes $\approx \pi f \Sigma_{\rm c}\Delta^2$ during this interval of τ. Tanigawa & Watanabe (2002) finds that for $\Delta \lesssim 0.1R_{\rm H}$, the accretion rate converges to a same steady rate regardless of what τ is initially chosen. A steady accretion rate

$$\dot{m}_{\rm p} = \frac{\pi f \Sigma_{\rm c}\Delta^2}{\tau} \tag{11}$$

is obtained to mimick the planet's actual gas accretion rate. For smaller τ, the converging timescale would be faster, as would the steady gas surface density in the gas removal zone. We adopt a standard sink hole radius of $0.1R_{\rm H}$ and $f/\tau = 5\Omega_{\rm p}$ (meaning the accretion is imposed at each artificial numerical timestep such that we take away $\sim 100\%$ of disk mass inside the sinkhole in a time of $0.2/\Omega_{\rm p}$). A convergence test is presented in §4.1 for different sink hole radii and timescales.

Table 1 shows the various model parameters for each simulation. All the numerical calculations are performed with a logarithmic mesh. The grid contains $n_r \times n_\varphi = 2048 \times 2048$ computational cells. It covers a disk in radial range from from $r_{\rm min} = 0.25\ a_{\rm p}$ to $r_{\rm max} = 8.0\ a_{\rm p}$. Unless otherwise stated for convergence tests, we use a standard sink hole radius and gas removal rate. For initial surface density, we adopt a standard scaled gas surface density with $\Sigma_{\rm p} = 10^{-3}$. The model parameters for comparison are $h_{\rm p}$, α and q.

In our simulations, we have fixed the planet's orbital radius. Because our simulation time is much shorter than the growth timescales, we also fix the planet mass. Each simulation is equivalent to taking a snapshot of a planet's steady accretion rate for a specified mass (Kley & Dirksen 2006). We focus on the effect of gap formation on the planets' accretion. We neglect here how planet migration might affect the streamlines within the CPD (D'Angelo et al. 2005).

4. SIMULATION RESULTS

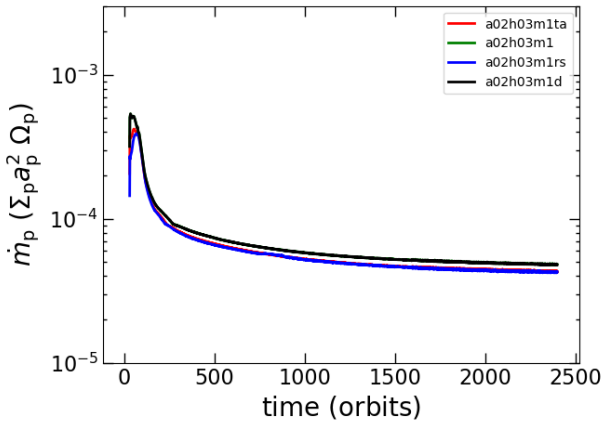

Figure 2. The evolution of planetary accretion rate, measured in scale-free unit $\Sigma_{\rm p}a_{\rm p}^2\Omega_{\rm p}$, of the convergence test runs. The model parameters are given in Table 1.

4.1. *Convergence test for the accretion rate*

In Figure 2 we present the evolution of planetary accretion rates for a standard a02h03m1 model with $\alpha = 1.11 \times 10^{-2}, h_{\rm p} = 0.03$, $q = 10^{-3}$. For convergence tests, we also introduce three variants using the same model parameters but different sink hole radius, removal rate, and initial surface density. Case a02h03m1rs has $\Delta = 0.05R_{\rm H}$, a02h03m1d has $\Sigma_{\rm p} = 10^{-4}M_*/a_{\rm p}^2$ and a02h03m1ta has $f/\tau = 2\Omega_{\rm p}$ respectively. The accretion rates converge to steady final values. They are measured in scale-free unit $\Sigma_{\rm p}a_{\rm p}^2\Omega_{\rm p}$ and they are shown in the $\dot{m}_{\rm p}$ column of Table 1. All four cases yield very similar steady dimensionless accretion rate, and demonstrate convergence for a) different sink hole radius as long as $\Delta \leq 0.1R_{\rm H}$; b) different f/τ and c) different $\Sigma_{\rm p}$. Indeed a) and b) are already confirmed in detail by Tanigawa & Watanabe (2002), and c) should be trivial as long as disk self-gravity is not invoked.

4.2. *Runaway growth with large disk eccentricities*

We list the numerical results on the accretion rates for all the models in the $\dot{m}_{\rm p}$ columns of Table 1. Similar to the convergence tests, most of the cases have a steady asymptotic accretion rate. However, some of the low viscosity models generate conspicuous growth and fluctuation of accretion rate, analogous to the findings of Kley & Dirksen (2006).

We plot in the upper panel of Figure 3 the evolution of planetary accretion rates for the a03h03m025, a03h03m1, a03h03m2, a03h03m4 cases with same viscosity/scale height ($[\alpha, h_{\rm p}]$=$[1.11 \times 10^{-3}, 0.03]$) but increasing planet mass (equivalently q). For $M_{\rm p} \leq M_{\rm J}$,

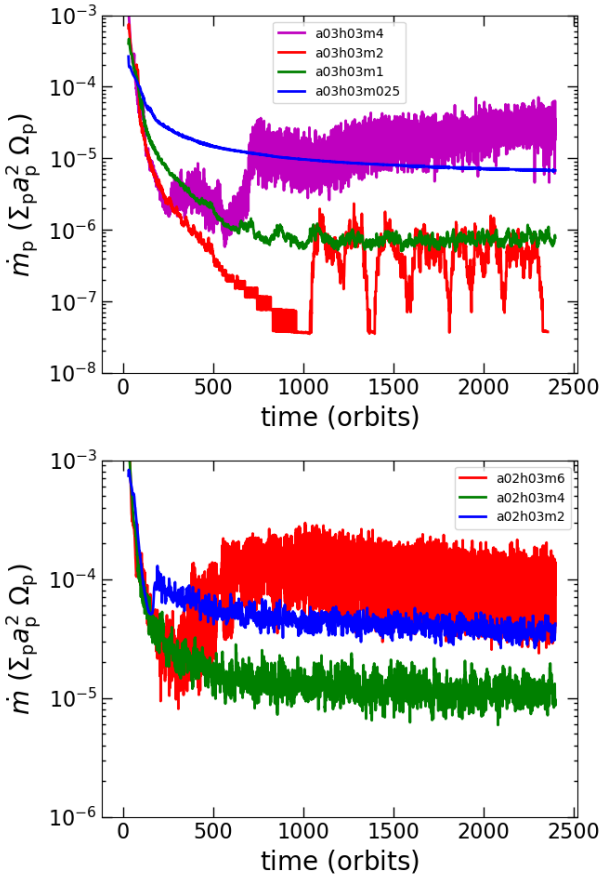

Figure 3. The evolution of planetary accretion rate, measured in scale-free units, of cases with $h_p = 0.03$ and $\alpha = 1.11 \times 10^{-3}$ (upper panel), and with $h_p = 0.03$ and $\alpha = 1.11 \times 10^{-2}$ (lower panel). The planet mass ratios for the upper panel, in increasing order, are $(0.25, 1, 2, 4) \times 10^{-3}$. The lower panel shows the planet mass ratios of $(2, 4, 6) \times 10^{-3}$. The last two cases in the upper panel and the last case in the lower panel show sudden rise and strong fluctuations of planetary accretion rates.

the planetary accretion rate evolves into steady values after more than 2400 orbits. However in the case of 2 M_J, 4 M_J, the accretion rate decays rapidly in the first 1000 orbits. It then abruptly jumps to much higher and more unstable values. Similar trend appears for the 4 M_J case with $h_p = 0.05, \alpha = 1.11 \times 10^{-3}$. In the lower panel of Figure 3, we show the evolution of planetary accretion rates for 2 M_J, 4 M_J and 6 M_J with $\alpha = 1.11 \times 10^{-2}$ and $h_p = 0.03$. This accretion rate fluctuation becomes more prominent at a higher planet mass ($\gtrsim 6\ M_J$). This pattern is directly associated with the excitation of streamlines' eccentricity and it should be distinguished from the orderly accreting process for lower-mass planets. The range for accretion fluctuation with the associated streamlines' eccentricity is highlighted in red in Table 1 for these cases.

Quantitatively, we compute the radial distribution of streamlines' eccentricity with the method introduced by Ogilvie (2001), (also see Kley & Dirksen 2006; Teyssandier & Ogilvie 2017). We follow the evolution of the peak eccentricities for streamlines in the vicinity of the planet's orbit for each case. Figure 4 shows the eccentricity evolution of most of the low-viscosity ($\alpha = 1.11 \times 10^{-3}$) cases. The top panel show the radial eccentricity distribution of disk gas at 2400 orbits, and the bottom panel shows the growth of the maximum eccentricity value within the disk in 2400 orbits. The disk eccentricity for a certain radius r is given by averaging the eccentricity for every cell at this radius, assuming the fluid elements are on Kepler orbits around the central star.

In this regime, we note that for a planet mass of $M_p = M_J$ in the $h_p = 0.03$ case, and for $M_p = 1$ & $2M_J$ in the $h_p = 0.05$ case, the peak eccentricities converge to a steady and stable value after ~ 2000 orbits. In the $M_p = 2$ and $4M_J$ with $h_p = 0.03$ cases and the $M_p = 4M_J$ with $h_p = 0.05$ case, the streamline eccentricity grows to be $\gtrsim R_H/a_p$ and the streamlines near the gap edge become unstable. In these cases, the planet's accretion rate does not converge to a steady value even after a few thousand orbits. The fluctuating eccentricities allow much more efficient angular momentum transfer and energy dissipation between crossing streamlines. They enhance the replenishment of materials into the planets' Hill radius during one dynamical time. These fluctuating cases cannot be accurately predicted by the existing analytic approximation of orderly-accretion scenarios. Regarding the tidal barrier, large fluctuation in eccentricity also breaks the time-independence of the flow structure, therefore the constraint inferred from the assumption of Bernoulli energy and vortensity conservation would be loosened.

For the high-viscosity ($\alpha = 1.11 \times 10^{-2}$) cases, we confirm the results of Kley & Dirksen (2006) that with $M_p \lesssim 6M_J$, the horseshoe streamlines are stable, albeit small eccentricities are excited. They suggest that for $\alpha = 0.01, h_p = 0.05$, a mass of $\gtrsim 5\ M_J$ is needed to excite sufficient eccentricity to "stir up" accretion whereas we found similar results for $M_p \gtrsim 6M_J$. For the $h_p = 0.03$ case, this threshold is lower and for $M_p \gtrsim 4M_J$ we already see the abnormal rise of planet accretion rate. However, our 2D results are in disagreement with the results of 3D nested-grid simulations by Bodenheimer et al. (2013). Their simulations do not indicate the onset of instability due to streamline eccentricity even in the high M_p line, for a medium viscosity $\alpha = 4 \times 10^{-3}$ that lies between our high and low cases. consequently the tidal barrier limit is always effective and their results

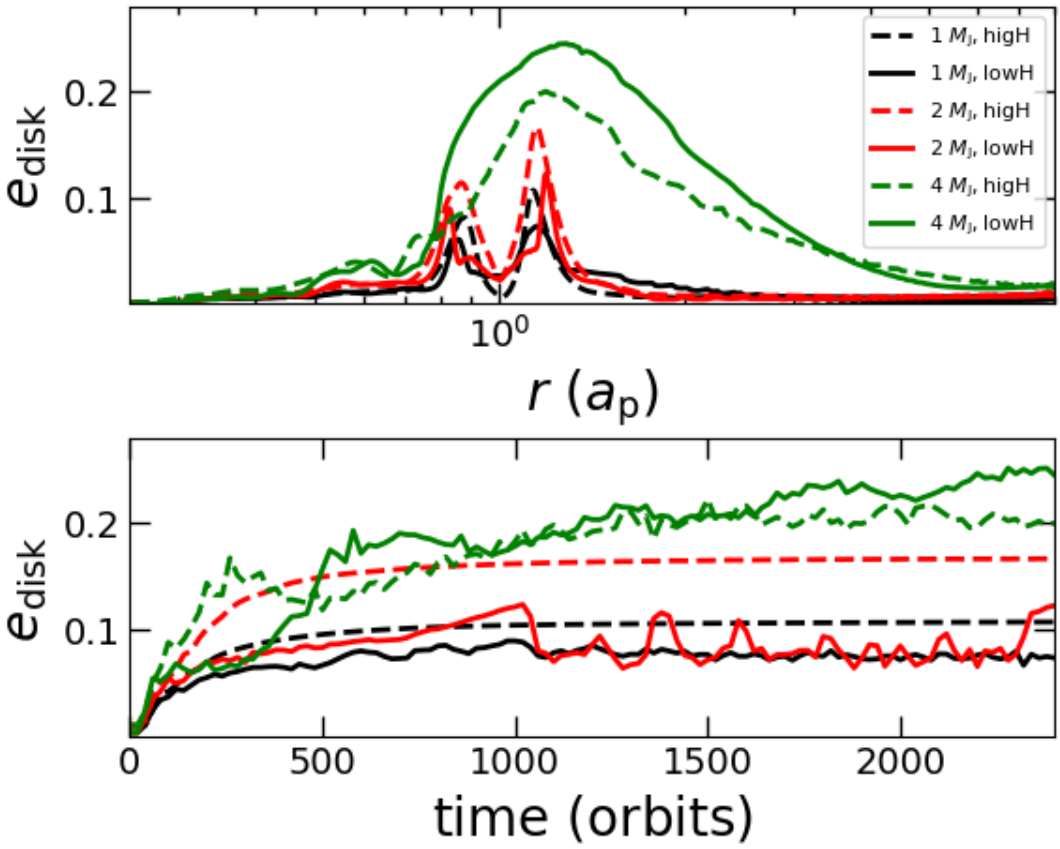

Figure 4. Top panel: The azimuthally averaged radial distribution of disk eccentricity at t=2400 orbits. Lower panel: the growth of the *peak* eccentricity within the disk over time. The solid lines represent the low disk scale height $h_p = 0.03$ cases, and the dashed lines represent the high scale height $h_p = 0.05$ cases.

matches with that predicted by the DLL prescription. The physical or computational reason for this dichotomy is not clear. We defer the investigation of this discrepancy elsewhere, and will focus on results from our 2D high resolution runs in the rest of this paper.

4.3. *Tidal Barrier for Jupiter-size Giants: Accretion Rates and Flow Patterns*

After distinguishing the cases with unstable streamline eccentricities and risen accretion rates, we compare the numerical results with predictions inferred from various prescriptions. This scrutiny is particularly relevant for models with orderly horseshoe streamlines and steady $\dot{m}_p$ which are the main focus of this paper. To show all of our results in the manner of Figure 1, we convert our dimensionless accretion rates into units of disk mass ($\Sigma_p a_p^2$) per *Earth year*, placing the planet on a fixed circular orbit with a semi major axis $a_p = 5$ au.

Four sets of different α and h_p are used in our simulations. The final accretion rates $\dot{m}_p$ from these simulations are plotted (in Figure 5) with the inferred values of $\dot{m}_p$ for the three prescriptions as a function of M_p (in units of Jupiter mass). Since the results of additional convergence tests are similar to those of the standard case, they are not shown here. For cases with large long-term fluctuations in the planets' accretion rates, we plot the medium value with solid red points and indicate the upper and lower bound with error-bars.

Results from the simulation agree well with the DLL tidal-barrier prescription in the low-viscosity ($\alpha = 1.11 \times 10^{-3}$) limit as it was intended. For relatively large $\alpha = 1.11 \times 10^{-2}$), viscous stress can lead to angular momentum transfer and energy dissipation across the tidal barrier. As gas distribution is smoothed over the gap region and inside the Hill radius (which is implicitly assumed by the RCGM prescription), the enhanced gas supply to the outer regions of the CPD elevates $\dot{m}_p$ onto the planets to values between those predicted by different prescriptions. Such high $\dot{m}_p$ may enable M_p to cross the threshold mass for the excitation of unstable streamline eccentricity, rapid diffusion of gas across the tidal barrier, and inflated $\dot{m}_p$. The growth of these planets' M_p (red dots) continues, until their natal PSD's are

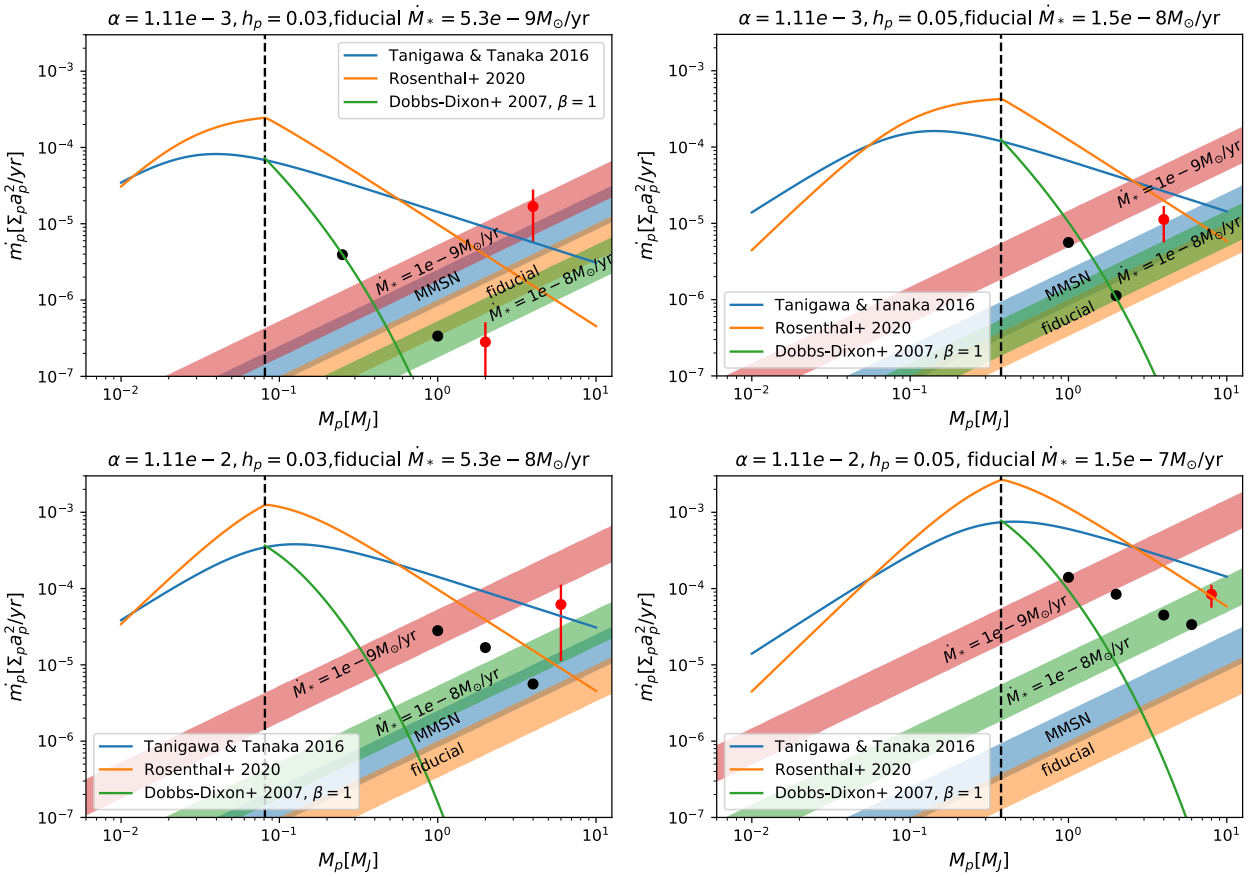

Figure 5. Planetary accretion rates as a function of planet mass in normalized units. Different color curves indication predictions of planet accretion rate as a function of planet mass $M_{\rm p}$, for four sets of $h_{\rm p}$ and α value. The black dots represent our numerical results for planet mass accretion rate. We add error-bars for the cases with unstable accretion rate and eccentricity. Color bands indicate where the growth timescale of the planet falls between 1-3 Myrs, for four different specific values for $\Sigma_{\rm p}/\dot{M}_*$.

severely depleted with an $\Sigma_{\rm p}$ less than that of MMSN , or $\dot{M}_* < 10^{-8} M_\odot$ yr^{-1}.

The conversion of $\dot{m}_{\rm p}$ in Figure 5 into physical units requires the specification of $\Sigma_{\rm p}$. The actual value of $\Sigma_{\rm p}$ in physical units can be inferred from α, $h_{\rm p}$, and the mass accretion rate $\dot{M}$ in the PSD (Equation 10). These values in physical units enable the determination of the characteristic growth time scale, $\tau_{\rm p} = M_{\rm p}/\dot{m}_{\rm p}$ for a protoplanet with a given mass $M_{\rm p}$. Inversely, we can infer the matching $\dot{M}_*$ or $\Sigma_{\rm p}$ required for any planet to acquire, but not to over-ingest, an asymptotic mass $M_{\rm p}$ within the typical PSD's depletion timescale ($\tau_{\rm dep} \simeq 2 \pm 1$ Myr) (Hartmann et al. 1998)).

We use four color bands to show this inversion (Figure 5), representing the range 1 Myr $< \tau_{\rm p} <$ 3 Myr. The orange color band represents a fiducial model in which we set $\Sigma_{\rm p} = 356$ g cm^{-1}, 2-3 times larger than the MMSN value (Hayashi 1981), such that the characteristic disk mass $\Sigma_{\rm p} a_{\rm p}^2 = M_{\rm J}$ (used as the standard in simulations). In comparison, the blue band represent the less massive MMSN model (Hayashi 1981). We also use pink, and green color bands to represent PSDs with disk accretion rates (Equation 10), $\dot{M}_* = 10^{-9}$ and $10^{-8} M_\odot$ yr^{-1} respectively. The value of $\dot{M}$ can be inferred directly from observation.

With a low viscosity ($\alpha = 1.11 \times 10^{-3}$), the planetary accretion rates of super-thermal planets $\dot{m}_{\rm p}$ are considerably lower than predicted by the TT or RCGM prescriptions either for $h_{\rm p} = 0.03$ or $h_{\rm p} = 0.05$. The $h_{\rm p} = 0.03$ case gives the lowest accretion rate in our simulations. For the fiducial (orange) or MMSN (blue) models, the mass-doubling timescale $\tau_{\rm p} = M_{\rm p}/\dot{m}_{\rm p} \sim 5$ Myrs for a $M_{\rm p} = M_{\rm J}$ protoplanet. Since $\tau_{\rm p} \gtrsim \tau_{\rm dep}$, the gas supply from the PSD would be depleted before the protoplanet can acquire sufficient mass to excite unstable streamline eccentricities. For the $h_{\rm p} = 0.05$ case which is more realistic for the MMSN (e.g. Garaud & Lin 2007), $\tau_{\rm p} > 1$ Myr for $M_{\rm p} = 2 M_{\rm J}$ planets in a fiducial or MMSN model. It is also possible for the growth of gap-opening planets to be quenched in such environments with modest masses before unstable streamline eccentricity is excited.

For each set of α and $h_{\rm p}$, the color $\dot{m}_{\rm p} - M_{\rm p}$ bands intercept the three different formulae (Figure 5). Dobbs-Dixon et al. (2007)'s tidal barrier prescription, if applicable, can account for emergence of planets with asymptotic mass comparable to that of Jupiter from natal disks with $\dot{M}_*$ comparable to that observed in typical disks around classical T Tauri stars. However, the TT and RCGM prescriptions predict much larger (by a factor of $\gtrsim 5$) asymptotic mass for emerging planets from identical PSDs. Equivalently, for the same growth limit, the PSDs need to be more severely depleted (with an order of magnitude smaller $\dot{M}$) in the TT, and RCGM prescriptions is larger than the DLL prescription.

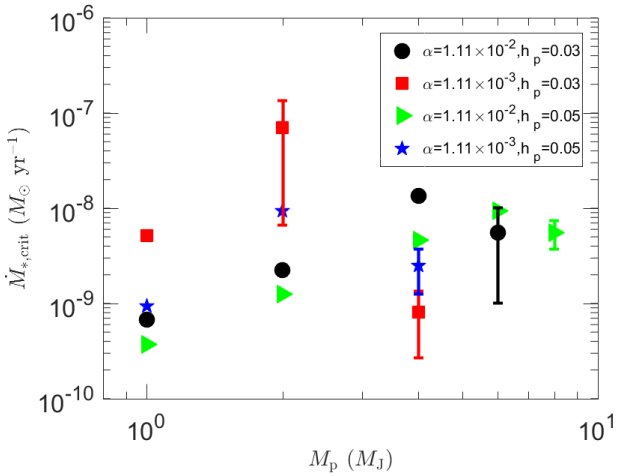

Figure 6. The required PSD accretion rate for planet mass doubling as a function of planet mass. The PSD accretion rate in this figure is estimated with a fixed depletion timescale of 3 Myr. The data points with error bars correspond to the cases where unstable accretions are involved.

An implication of the numerical results is well illustrated by the upper limit of $\dot{M}_*$ that can *prevent* planets from doubling their $M_{\rm p}$ over 3 Myr in a steady state disk (Figure 6), denoted as $\dot{M}_{*,\rm crit}$. Various values of the model parameters α and $h_{\rm p}$ are denoted by different symbols. The low-viscosity ($\alpha = 1.11\times10^{-3}$) cases show a peak $\dot{M}_{*,\rm crit}(\sim 10^{-8} - 10^{-7} M_\odot$ yr^{-1}) around 2 $M_{\rm J}$. For the high-viscosity ($\alpha = 1.11\times10^{-2}$) cases, this peak $\dot{M}_{*,\rm crit}(\sim 10^{-8} M_\odot {\rm yr}^{-1})$ is around 4-6 $M_{\rm J}$. Since this range of $\dot{M}_{*,\rm crit}$ is comparable to that observed among PSDs around a few Myr old classical T Tauri stars, the runaway growth of protoplanets may indeed be halted with masses comparable to Jupiter. In disks with larger $\dot{M}_*(> \dot{M}_{*,\rm crit})$ or $\tau_{\rm dep}(\gtrsim 3{\rm Myr})$, $M_{\rm p}$ may continue to increase until unstable streamline eccentricity is excited. Such massive planets (with $M_{\rm p} > 4M_{\rm J}$) have smaller growth-quenching $\dot{M}_{*,\rm crit}(\lesssim 10^{-9} M_\odot {\rm yr}^{-1})$ and their $M_{\rm p}$ continues to increase until their natal disk is globally depleted by either planetary consumption or outflow. (Local gas depletion in the gap may not be adequate to quench planet's growth by gas supply from other regions of the disk).

With relatively large ($\alpha = 1.11\times10^{-2}$) viscosity (lower panels of Figure 5, also see §4.4), however, the tidal barrier is overrun. Viscous diffusion leads to a greater flux of gas supply from 1) the outer PSD onto the horseshoe streamlines, 2) horseshoe streamlines at the edge of the gap towards the interior of the gap near the L_4 and L_5 points, and 3) most importantly, horseshoe streamlines to the outer region of the CPD. These flow pattern produces the boundary conditions assumed by the TT and RCGM prescriptions such that the values of $\dot{m}_{\rm p}$ from the numerical simulations come towards their predicted values.

In strongly viscous PSD's around classical T Tauri stars (with $\dot{M}_* \sim 10^{-8} M_\odot$ yr^{-1}), $M_{\rm p}$ can reach $\sim 4M_{\rm J}$ without the excitation of unstable streamline eccentricity (in contrast to the low-viscosity cases). But, planets with $M_{\rm p}(\gtrsim 5{-}8M_{\rm J})$ do excite unstable streamline eccentricity even in the high α limit as we summarise in Table 1 (also see Kley & Dirksen 2006). Transition to unstable streamline eccentricity further enhance the planets' accretion rate $\dot{m}_{\rm p}$, reduce the growth-quenching $\dot{M}_*$, promote planets' asymptotic masses to become much larger than that of Jupiter.

Nevertheless, the growth of planets can be halted at $M_{\rm p} \sim 1 - 2M_{\rm J}$ in the high-viscosity limit with $\dot{M}_*(\sim 10^{-9} M_\odot {\rm yr}^{-1})$ comparable to or smaller than that found in PSD's during some advanced evolutionary stages including 1) those around weak-line T Tauri stars (Figure 6) or 2) in transitional disks during the brief epochs of rapid gas depletion. Such finely-tuned and promptly-timed coincidence between the emergence of gas giant planets and the clearing of their natal environment (Tanaka et al. 2020) may introduce some challenges to explain the observed mass function of exoplanets, especially around multiple-gas-giant-planet bearing stars (see discussions in §2).

4.4. *Flow near planet's Hill sphere*

The presence of a tidal barrier is best illustrated with velocity-arrow plots and with vortensity contours in the planetary proximity. The vortensity (or potential vorticity; PV) is defined as (Papaloizou & Lin 1989; Korycansky & Papaloizou 1996):

$$\varpi = \frac{\omega + 2\Omega_{\rm p}}{\Sigma}, \tag{12}$$

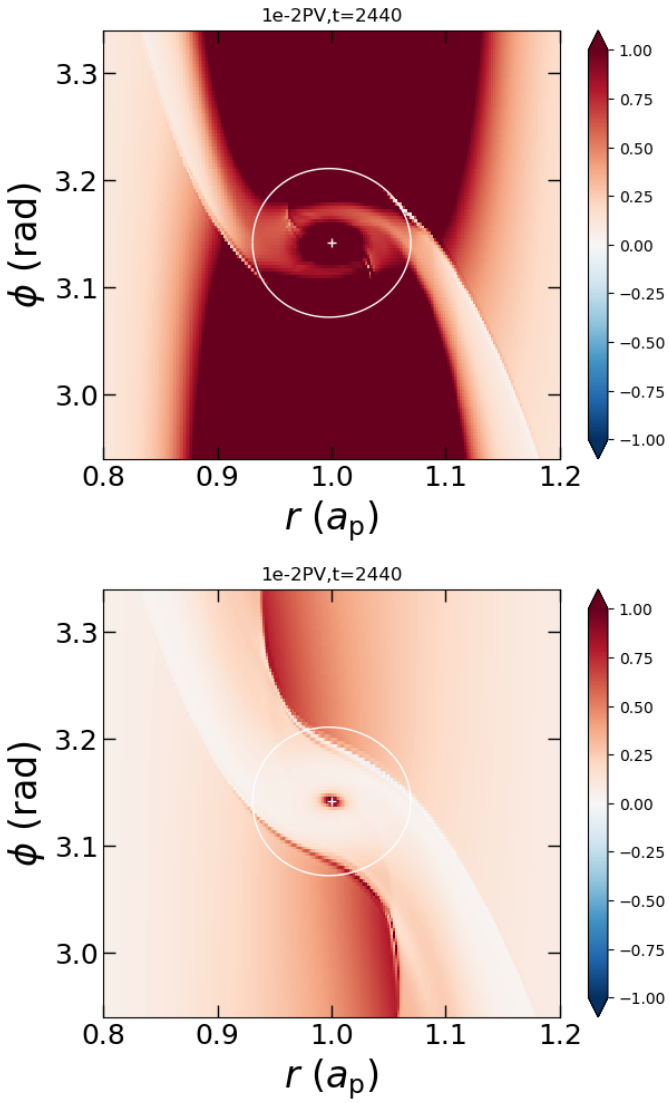

Figure 7. The vortensity ϖ distribution around the location of the planet. Upper panel: $M_{\rm p} = M_{\rm J}$, $h_{\rm p} = 0.05$, low viscosity case; Lower panel: $M_{\rm p} = M_{\rm J}$, $h_{\rm p} = 0.05$, high viscosity case. The circle around the planet has a radius of $R_{\rm H}$. 1e-2PV means that the value of vortensity shown in this plot is 1% of the actual value (in dimensionless units) for the purpose of illustration.

where ω is the vertical component of the vorticity, which is defined as

$$\omega = \hat{z} \cdot \nabla \times \vec{v}. \tag{13}$$

In the absence of shock dissipation and viscous diffusion, the vortensity is conserved along streamlines. Moreover, there is generally a mismatch of vortensity between the flow in the outer boundary of the CPD and the horseshoe streamlines that are deflected away from the CPD even though their interface is inside the Hill radius (Korycansky & Papaloizou 1996).

In Figure 7 we compare the vortensity around the planet for case a03h05m1 and a02h05m1 after 2440 orbits. In the first case there is a small viscosity ($\alpha = 1.11 \times 10^{-3}$, upper panel) such that the vortensity is not strictly but approximately conserved along streamlines. Sharp transitions in the vortensity distribution across the CPD-horseshoe streamline interface is evident. However, for large viscosity ($\alpha = 1.11 \times 10^{-2}$, lower panel) case, viscous transport and energy dissipation smooth the distribution of vortensity across these interfaces. Accordingly, the tidal barrier for the diffusion of gas in horseshoe streamlines onto the outer regions of the CPD is partially unblocked.

In order to show the flow pattern of materials across the planet's orbit, we uniformly insert a thin layer of very small (2μm) tracer particles outside (at $r > 1.2a_{\rm p}$) the gap region. They are released at t=2400 orbits after the disk has attained an asymptotic steady gap structure. These particles are well coupled to the gas and do not have any feedback effect on the disk gas, similar to the scalar dye used by Duffell et al. (2014). They are employed as a passive contaminant to characterize the flow pattern. We follow the surface-density and velocity evolution of these particles as they flow into and across the gap region.

Figure 8 shows the surface density $\Sigma_{\rm d}$ and velocity field of these tracer particles, at 40 planetary orbital periods after their initial installment. The upper and lower panels are for the low and high viscosity cases (a03h05m1 and a02h05m1 respectively). In both models, $h_{\rm p} = 0.05$. In the low-viscosity case, the tracer particles from the outer disk diffuse onto a narrow strand of horseshoe streamlines analogous to the solar system asteroids which share Jupiter's orbit. These tracer particles do not reach the interior region of the gap (at $r \simeq a_{\rm p}$ and in azimuth away from the planet). As the streamlines approaches to the planet, their courses are deflected by the planet's gravitational perturbation and the Coriolis force associated with the rotating frame. Their paths first diverge outside the planet's Hill sphere along the surface of vortensity discontinuity, between the trailing density waves and the narrowly-confined horseshoe streamlines around the L_4 and L_5 points in the Roche equipotential surfaces.[2] Gas on the horseshoe

[2] In isolation, local viscous diffusion and energy dissipation around these potential maxima would lead to gas flowing away from them (Lin et al. 1987) unless there are additional viscous stress (exerted by PSD beyond the gap) or external tidal torque (due to other planets) to fill in the gap region. While Fig 8 only show the velocity of incoming tracers at a narrow azimuthal region, horseshoe flows of residual gas circulating L4 & L5 points can be directly seen in Figure 9 of Chen et al. (2020b).

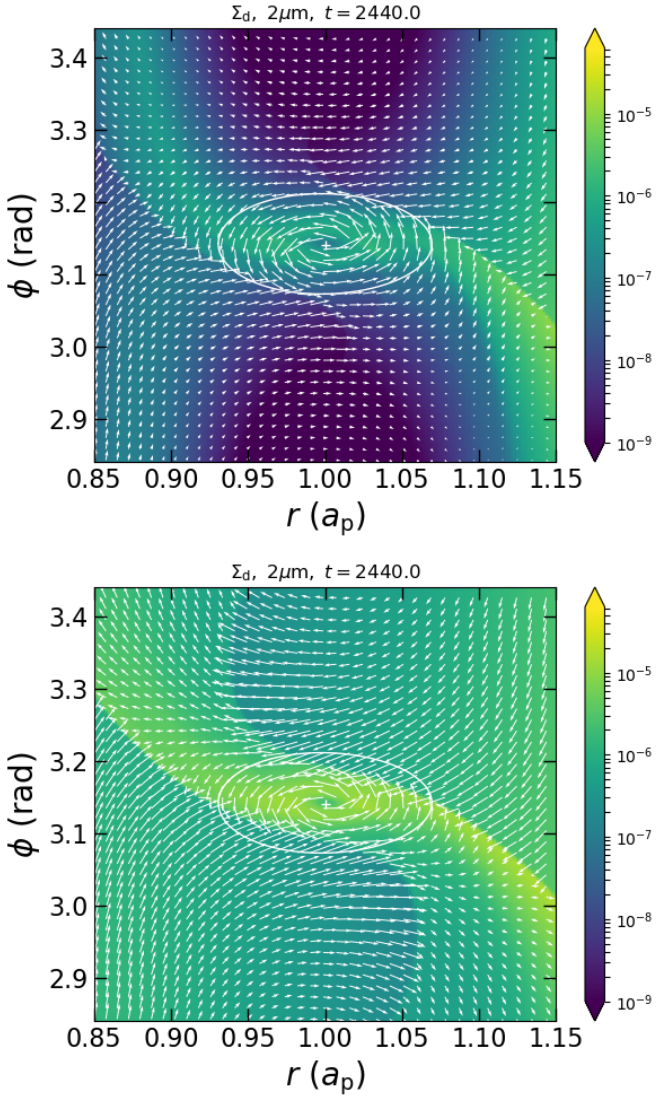

Figure 8. The surface density contour and the velocity field in the rotating frame of the planet for tracer particles. The color represents the surface density of 2μm tracer particles at t=2440 orbits. The particles are uniformly released outside $1.2a_p$ after the gap has formed, and completely couple with the gas flowing into the gap region. The arrows show the velocity field of the tracer. Upper panel: $M_p = M_J$, $h_p = 0.05$, low viscosity case; Lower panel: $M_p = M_J$, $h_p = 0.05$, high viscosity case. The circle around the planet has a radius of R_H.

streamlines flows across the gap, diffuses into regions of the PSD interior to a_p, and preserves a steady $\dot{M}$ towards the central star. This flow pattern enable the gas to maintain a steady Σ distribution. The associated torque density determines the pace and direction of the planet's type II migration (Chen et al. 2020b).

Inside the protoplanet's Hill sphere, the horseshoe streamlines converge with those near the outer boundary of the CPD. There are also vortensity discontinuity and shear across their interface. Viscous transfer of angular momentum (relative to the protoplanet) enables a small fraction of the intercepting horseshoe streamlines to join onto the CPD. This fresh supply of gas is diffused to the surface of the planet through the viscous transfer of angular momentum in the CPD. In the low-viscosity limit, the mass flux through these region is relatively low.

In the strongly-viscous case, the high efficiency of angular momentum transfer leads to mass diffusion from materials outside a_p well into the gap region. After 2440 orbits, the tracers' density Σ_d is nearly uniform. Relatively large viscosity also enhance angular momentum transfer and mass diffusion across the interface between horseshoe streamlines and CPD. Consequently the vortensity gradient is smoothed out such that the obstruction of gas flow across the tidal barrier and onto the CPD is reduced. These effects elevate the mass supply onto the CPD and eventually accretion into the sink hole.

Similar flow pattern of the gas have also been noted by Lubow et al. (1999) and Miyoshi et al. (1999). We reiterate Dobbs-Dixon et al. (2007)'s conclusions that the physical meaning behind the separation of flows is the mismatch of vortensity. The streamline/velocity plots for the tracer particles that are added to couple with the gas *after* the formation of the gap provide more clear illustration on the nature of the accretion flows, especially for low-viscosity cases, by avoiding the interference of horseshoe flow around L_4 & L_5 points that's irrelevant to incoming materials.

5. SUMMARY

In this paper, we performed extensive numerical simulations to study the dynamical accretion of gas giants. Some previous works (Tanigawa & Tanaka 2016; Rosenthal et al. 2020) have estimated the asymptotic masses of gas giants, with empirical & semi-analytical TT and RCGM prescription. These formulae predict that the accretion rates falls off as power-law functions of M_p after the planets have become sufficiently massive to open up gaps in their natal disks near their orbital semi major axis. In the determination of $\dot{m}_p$, the tidal perturbation of the host star inside the planets' Hills radius is generally neglected. Moreover, the background is assumed to be provided by the residual gas along the horseshoe streamlines with the lowest residual surface density found from numerical simulation and analytic modeling (Duffell & MacFadyen 2013; Kanagawa et al. 2015), and the surface density is averaged in azimuth under the implicit assumption of axial symmetry. Un-

der these assumptions, only deep gap-clearing or severe global depletion could quench the accretion onto the planet. In disks with moderate or large viscosity, these prescriptions predict typical asymptotic masses $\gtrsim 10 M_{\rm J}$ which is difficult to reconcile with observational data. In addition, the mass ratio of such planets to their host stars $q(\gtrsim 0.005)$ exceeds the critical values which can lead to the excitation of unstable streamline eccentricity (e.g. Kley & Dirksen 2006; Teyssandier & Ogilvie 2017; Duffell & Chiang 2015) and further elevation of planets' accretion rate and asymptotic masses.

In contrast, Dobbs-Dixon et al. (2007) used analytical approximations and 2D numerical simulations to show that, in the low-viscosity or inviscid limit, the conservation of Bernoulli energy and vortensity of gas streamlines around the planet contribute together to impose a tidal barrier. Inside the planet's Hill sphere, the gas streamlines are deflected by the host stars' tidal perturbation and the Coriolis force from the frame which corotates with the orbit of the planet. The tidal barrier separates the incoming horseshoe streamlines from those on the CPD. Across the separatrix, there is a vortensity discontinuity. Viscous stress due to either intrinsic viscosity or shock dissipation leads to angular momentum transfer, and the diffusion of a small fraction of gas on the incoming horseshoe streamlines onto the outer regions of the CPD. This continuous influx of gas is eventually accreted by the planet as it viscously diffuses through the CPD.

Dobbs-Dixon et al. (2007) has numerically tested this theory in inviscid disks. They also introduced a DLL prescription for the planets' asymptotic mass. We carry out a series of models with a range of aspect ratio and viscosity. The relevance of $h_{\rm p}$ is clearly stated in Equation 5. The magnitude of α is also important in regulating the rate of angular momentum transfer and mass diffusion 1) between the horseshoe streamlines and PSD outside (and inside) the gap and 2) across the tidal barrier between horseshoe streamlines and CPDs.

In Table 1 we summarize the simulation parameters and the normalized planetary accretion rates for all of our models. We compare the numerical results with various prescriptions. In low-viscosity disks, the relation between stable-eccentricity accretion rate and planet mass conform more with exponential decay as predicted by the DLL prescription than the linear scalings from the TT and RCGM prescription. For high-viscosity disks, the tidal barrier is overcome by diffusion and dissipation such that the decline in $\dot{m}_{\rm p}$ for increasing $M_{\rm p}$ is less steep. We used vortensity contours and tracer velocity arrowplots to show that the "barrier" deflecting accreting streamlines is directly associated with the distribution of vortensity. We are aware that Tanaka, Yuki., et al. (in prep) are performing a parallel numerical study on orderly & eccentric accretion of gas giants, nevertheless their focus is different from the tidal barrier.

When appropriate scaling for physical parameters is applied, overgrown gas giants (with $M_{\rm p} \gg M_{\rm J}$) can be avoided in PSDs around classical T Tauri stars provided their $\alpha \sim 10^{-3}$ and $h_{\rm p} \sim 0.03 - 0.05$. In this low-viscosity limit, the tidal barrier model is appropriate prescription for the asymptotic mass of planets. In highly viscous disks (with $\alpha \sim 10^{-2}$), the tidal barrier is no longer effective and the asymptotic mass of planets formed in orderly disks around classical T Tauri stars are typically several times more massive than Jupiter. Similarly, thicker disks imply larger $q_{\rm th}$ and super Jupiter masses. Such massive planets may excite unstable streamline eccentricity, enhance angular momentum transfer and mass supply to the outer regions of CPD and further elevate the asymptotic mass of gas giant planets to more than an order of magnitude larger than that of Jupiter. Based on these inference and the observed mass distribution of exoplanets, we speculate that most Jupiter-mass planets are formed in PSDs with relatively low $\alpha(\sim 10^{-3})$.

For the theoretical predictions in Figures 1 and 5, we have extended the Duffell & MacFadyen (2013); Kanagawa et al. (2015) gap-scaling of $\Sigma_{\rm min}$ to at least 4 $M_{\rm J}$ to compare with our numerical results, as in Tanigawa & Tanaka (2016). There is no physical reason to justify the extrapolation of this scaling law beyond the gap opening limit since the Lindblad torques at the edges of the gap no longer uniformly scales with the bottom density. Empirically, it can still be used to inferred the average torque density winthin an order unity provided there is still some residual gas flowing across the gap (Chen et al. 2020b). A more accurate analytical surface density formulae for gap-opening planets needs to be constructed in order to reduce this uncertainty in the future. We note that if this gap scaling law overestimates $\Sigma_{\rm min}$ for the gap-opening planets, the planetary accretion rates would be smaller. It would also imply smaller (and usually more realistic) asymptotic masses for gas giants. Although we have shown numerically that the effectiveness of the tidal barrier is diminished by viscous dissipation, an analytical model on how tidal barrier can be partially overcome in the presence of viscosity is left for subsequent studies.

In our numerical simulations, we neglect the feedback torque of the disk gas on the planet's orbit. Both orbital migration and eccentricity excitation may lead to additional diffusion across the gap as well as the interface which separates the horseshoe streamlines and

the CPD (D'Angelo et al. 2005; D'Angelo & Lubow 2008). The surface density distribution across the gap determines the density of both Lindblad and corotation torque (Chen et al. 2020b). The large ratio (~ 10) between the observed frequency of cold versus hot Jupiters indicate that the extent of migration may be limited. The eccentricity of some planets with $M_{\rm p} \gg M_{\rm J}$ and $a_{\rm p} \gtrsim$ a few au may be due to planet-disk interaction as well as dynamical instability in multiple-planet systems. These feedback effects will be examined in subsequent studies.

We have used global 2D high-resolution simulations in this study. While this approximation captures the vertically averaged flow patterns of the gas around the planet, it may have excluded some important physical effects. Szulágyi et al. (2014) finds that certain mechanisms in an inviscid 3D CPD structure can also quench planet growth, when the planet is actually fed by meridional flows that transport materials to its poles (Fung & Chiang 2016). In particular, results from 3D nested-grid simulations of Bodenheimer et al. (2013) does not show abnormal rise of accretion rate for $M_{\rm p} \gtrsim 5\ M_{\rm J}$ resulting from the excited streamline eccentricity. Their results contradict the conclusions of many global 2D simulations (Kley & Dirksen 2006; Duffell & Chiang 2015; Teyssandier & Ogilvie 2017) as well as our results. Additional high-resolution global 3D simulations need to be carried out to investigate this discrepancy in details. Nevertheless, the polar accretion effect and the damping of eccentricity in 3D, if they are due to physical instead of numerical reasons, would both disfavor high $\dot{m}_{\rm p}$ and asymptotic masses. Combined with the conservation of vortensity and Bernoulli energy along streamlines, they should make quenching of runaway growth more robust.

ACKNOWLEDGMENTS

We thank Eugene Chiang, Chris Ormel, Gordon Ogilvie, Hidekazu Tanaka, Xiaojia Zhang, Hui Li, and Judit Szulagyi for helpful discussions. We thank Yuki Tanaka for sharing information about their paper in preparation. Y.P.L. gratefully acknowledges the support by LANL/LDRD. This research used resources provided by the Los Alamos National Laboratory Institutional Computing Program, which is supported by the U.S. Department of Energy National Nuclear Security Administration under Contract No. 89233218CNA000001. Softwares: `LA-COMPASS` (Li et al. 2005, 2009), `Numpy` (van der Walt et al. 2011), `Matplotlib` (Hunter 2007)

REFERENCES

Ali-Dib, M., Cumming, A., & Lin, D. N. C. 2020, MNRAS, 494, 2440, doi: 10.1093/mnras/staa914

Andrews, S. M., Huang, J., Pérez, L. M., et al. 2018, ApJL, 869, L41, doi: 10.3847/2041-8213/aaf741

Balmforth, N. J., & Korycansky, D. G. 2001, MNRAS, 326, 833, doi: 10.1046/j.1365-8711.2001.04619.x

Bodenheimer, P., D'Angelo, G., Lissauer, J. J., Fortney, J. J., & Saumon, D. 2013, ApJ, 770, 120, doi: 10.1088/0004-637X/770/2/120

Bodenheimer, P., & Pollack, J. B. 1986, Icarus, 67, 391, doi: 10.1016/0019-1035(86)90122-3

Bryden, G., Chen, X., Lin, D. N. C., Nelson, R. P., & Papaloizou, J. C. B. 1999, ApJ, 514, 344, doi: 10.1086/306917

Chen, Y.-X., Li, Y.-P., Li, H., & Lin, D. N. C. 2020a, ApJ, 896, 135, doi: 10.3847/1538-4357/ab9604

Chen, Y.-X., Zhang, X., Li, Y.-P., Li, H., & Lin, D. N. C. 2020b, arXiv e-prints, arXiv:2007.14905. https://arxiv.org/abs/2007.14905

Crida, A., Morbidelli, A., & Masset, F. 2006, Icarus, 181, 587, doi: 10.1016/j.icarus.2005.10.007

Cumming, A., Butler, R. P., Marcy, G. W., et al. 2008, PASP, 120, 531, doi: 10.1086/588487

D'Angelo, G., Bate, M. R., & Lubow, S. H. 2005, MNRAS, 358, 316, doi: 10.1111/j.1365-2966.2005.08866.x

D'Angelo, G., Kley, W., & Henning, T. 2003, ApJ, 586, 540, doi: 10.1086/367555

D'Angelo, G., & Lubow, S. H. 2008, ApJ, 685, 560, doi: 10.1086/590904

de Val-Borro, M., Edgar, R. G., Artymowicz, P., et al. 2006, MNRAS, 370, 529, doi: 10.1111/j.1365-2966.2006.10488.x

Dobbs-Dixon, I., Li, S. L., & Lin, D. N. C. 2007, ApJ, 660, 791, doi: 10.1086/512537

Duffell, P. C. 2015, ApJL, 807, L11, doi: 10.1088/2041-8205/807/1/L11

—. 2020, ApJ, 889, 16, doi: 10.3847/1538-4357/ab5b0f

Duffell, P. C., & Chiang, E. 2015, ApJ, 812, 94, doi: 10.1088/0004-637X/812/2/94

Duffell, P. C., Haiman, Z., MacFadyen, A. I., D'Orazio, D. J., & Farris, B. D. 2014, ApJL, 792, L10, doi: 10.1088/2041-8205/792/1/L10

Duffell, P. C., & MacFadyen, A. I. 2013, ApJ, 769, 41, doi: 10.1088/0004-637X/769/1/41

Dürmann, C., & Kley, W. 2015, A&A, 574, A52, doi: 10.1051/0004-6361/201424837

Frank, J., King, A., & Raine, D. 1992, Accretion power in astrophysics., Vol. 21
Fung, J., & Chiang, E. 2016, ApJ, 832, 105, doi: 10.3847/0004-637X/832/2/105
Fung, J., Shi, J.-M., & Chiang, E. 2014, ApJ, 782, 88, doi: 10.1088/0004-637X/782/2/88
Garaud, P., & Lin, D. N. C. 2007, ApJ, 654, 606, doi: 10.1086/509041
Ginzburg, S., & Chiang, E. 2019, MNRAS, 487, 681, doi: 10.1093/mnras/stz1322
Ginzburg, S., & Sari, R. 2018, MNRAS, 479, 1986, doi: 10.1093/mnras/sty1466
Goldreich, P., & Tremaine, S. 1980, ApJ, 241, 425, doi: 10.1086/158356
Hartmann, L., Calvet, N., Gullbring, E., & D'Alessio, P. 1998, ApJ, 495, 385, doi: 10.1086/305277
Hayashi, C. 1981, Progress of Theoretical Physics Supplement, 70, 35, doi: 10.1143/PTPS.70.35
Hunter, J. D. 2007, Computing in Science and Engineering, 9, 90, doi: 10.1109/MCSE.2007.55
Ida, S., & Lin, D. N. C. 2004, ApJ, 604, 388, doi: 10.1086/381724
Ida, S., Lin, D. N. C., & Nagasawa, M. 2013, ApJ, 775, 42, doi: 10.1088/0004-637X/775/1/42
Kanagawa, K. D., Tanaka, H., Muto, T., Tanigawa, T., & Takeuchi, T. 2015, MNRAS, 448, 994, doi: 10.1093/mnras/stv025
Kley, W., D'Angelo, G., & Henning, T. 2001, ApJ, 547, 457, doi: 10.1086/318345
Kley, W., & Dirksen, G. 2006, A&A, 447, 369, doi: 10.1051/0004-6361:20053914
Korycansky, D. G., & Papaloizou, J. C. B. 1996, ApJS, 105, 181, doi: 10.1086/192311
Lee, E. J., & Chiang, E. 2015, ApJ, 811, 41, doi: 10.1088/0004-637X/811/1/41
Lee, E. J., Chiang, E., & Ormel, C. W. 2014, ApJ, 797, 95, doi: 10.1088/0004-637X/797/2/95
Li, H., Li, S., Koller, J., et al. 2005, ApJ, 624, 1003, doi: 10.1086/429367
Li, H., Lubow, S. H., Li, S., & Lin, D. N. C. 2009, ApJL, 690, L52, doi: 10.1088/0004-637X/690/1/L52
Lin, D. N. C., Bodenheimer, P., & Richardson, D. C. 1996, Nature, 380, 606, doi: 10.1038/380606a0
Lin, D. N. C., & Papaloizou, J. 1986a, ApJ, 307, 395, doi: 10.1086/164426
—. 1986b, ApJ, 309, 846, doi: 10.1086/164653
Lin, D. N. C., & Papaloizou, J. C. B. 1993, in Protostars and Planets III, ed. E. H. Levy & J. I. Lunine, 749–835
Lin, D. N. C., Papaloizou, J. C. B., & Ruden, S. P. 1987, MNRAS, 227, 75, doi: 10.1093/mnras/227.1.75
Long, F., Pinilla, P., Herczeg, G. J., et al. 2018, ApJ, 869, 17, doi: 10.3847/1538-4357/aae8e1
Lubow, S. H., Seibert, M., & Artymowicz, P. 1999, ApJ, 526, 1001, doi: 10.1086/308045
Machida, M. N., Kokubo, E., Inutsuka, S.-I., & Matsumoto, T. 2010, MNRAS, 405, 1227, doi: 10.1111/j.1365-2966.2010.16527.x
Marcy, G., Butler, R. P., Fischer, D., et al. 2005, Progress of Theoretical Physics Supplement, 158, 24, doi: 10.1143/PTPS.158.24
Mayor, M., Marmier, M., Lovis, C., et al. 2011, arXiv e-prints, arXiv:1109.2497. https://arxiv.org/abs/1109.2497
Miyoshi, K., Takeuchi, T., Tanaka, H., & Ida, S. 1999, ApJ, 516, 451, doi: 10.1086/307086
Murray, C. D., & Dermott, S. F. 1999, Solar system dynamics
Ogilvie, G. I. 2001, MNRAS, 325, 231, doi: 10.1046/j.1365-8711.2001.04416.x
Ormel, C. W., Shi, J.-M., & Kuiper, R. 2015, MNRAS, 447, 3512, doi: 10.1093/mnras/stu2704
Owen, J. E., Ercolano, B., & Clarke, C. J. 2011, MNRAS, 412, 13, doi: 10.1111/j.1365-2966.2010.17818.x
Papaloizou, J. C. B., & Lin, D. N. C. 1989, ApJ, 344, 645, doi: 10.1086/167832
Petigura, E. A., Marcy, G. W., Winn, J. N., et al. 2018, AJ, 155, 89, doi: 10.3847/1538-3881/aaa54c
Piso, A.-M. A., & Youdin, A. N. 2014, ApJ, 786, 21, doi: 10.1088/0004-637X/786/1/21
Pollack, J. B., Hubickyj, O., Bodenheimer, P., et al. 1996, Icarus, 124, 62, doi: 10.1006/icar.1996.0190
Regály, Z., Sándor, Z., Dullemond, C. P., & van Boekel, R. 2010, A&A, 523, A69, doi: 10.1051/0004-6361/201014427
Rosenthal, M. M., Chiang, E. I., Ginzburg, S., & Murray-Clay, R. A. 2020, MNRAS, doi: 10.1093/mnras/staa1721
Shakura, N. I., & Sunyaev, R. A. 1973, A&A, 500, 33
Szulágyi, J., Morbidelli, A., Crida, A., & Masset, F. 2014, ApJ, 782, 65, doi: 10.1088/0004-637X/782/2/65
Tanaka, H., Murase, K., & Tanigawa, T. 2020, ApJ, 891, 143, doi: 10.3847/1538-4357/ab77af
Tanigawa, T., & Ikoma, M. 2007, ApJ, 667, 557, doi: 10.1086/520499
Tanigawa, T., & Tanaka, H. 2016, ApJ, 823, 48, doi: 10.3847/0004-637X/823/1/48
Tanigawa, T., & Watanabe, S.-i. 2002, ApJ, 580, 506, doi: 10.1086/343069
Teyssandier, J., & Ogilvie, G. I. 2016, MNRAS, 458, 3221, doi: 10.1093/mnras/stw521
—. 2017, MNRAS, 467, 4577, doi: 10.1093/mnras/stx426

van der Walt, S., Colbert, S. C., & Varoquaux, G. 2011,
Computing in Science and Engineering, 13, 22,
doi: 10.1109/MCSE.2011.37